Exploring the electrical and magnetic characteristics of novel barium-doped bismuth ferrite ($Bi_{0.9}Ba_{0.1}FeO_3$) nanocomposites and their applications for electrocatalytic degradation of Congo red dye

M. H. Ghozza,[a] Tarek A. Yousef,[b] Abdullah Al-Dakhil,[b] Hela Ferjani,[c] Abeer M. Alosaimi,[d] Reda Abdel-Hameed, [e] Elbadawy A. Kamoun, [*f] H. Y. Zahran,[g] Ahmed T. Mosleh [h] and I. S. Yahia[*g]

Bismuth perovskite $Bi_{0.9}Ba_{0.1}FeO_3$ nanoparticles were synthesized by a solution-combustion technique at a fuel-to-oxidizer ratio equal to unity ($\varnothing = (F/O) = 1$), where the effect of fuel type on their structural, electric, magnetic, and photocatalytic properties was discussed. Using Rietveld refinement with FullProf software, the prepared materials were characterized by XRD and SEM to examine their composition and morphology. Results revealed that the perovskite's pure phase ranged from 74% to 100%. Meanwhile, Scherrer, Williamson–Hall, and SEM investigations were used to calculate the crystallite sizes of the samples, which ranged from 18.5–27.7 nm, 23–32 nm, 23.8–34.3 nm, and 53.8–292.8 nm, respectively. In addition, the increase in DC conductivity is explained by decreased grain boundary scattering, due to the reduction of crystallite size. The multiferroic nanoparticles' estimated activation energy ranged from 0.39 to 0.07 eV. The transition temperature was 368 K for urea and triethanolamine (TEA) samples, while the other samples were pushed to a lower temperature, where conduction followed non-adiabatic small polaron hopping (SPH). Meanwhile, TEA and fuel-free samples appear to have a high magnetization parameter. The coercivity Hc of the TEA sample is three times greater than the others. According to the tests conducted to assess the nanoparticles' electrocatalytic performances, every fuel utilized in nanoparticle production process significantly impacts the electrocatalytic degradation of Congo red (CR) dye. When the 4 minutes experiment was over, all dye content in the solution was eliminated. The synthesized $Bi_{0.9}Ba_{0.1}FeO_3$ using various fuels considerably impacts the parameters under study. Therefore, appropriate magnetic, electrical, and electrocatalysis properties were achieved by modifying the fuel type.

[a]*Basic Science Department, Cairo Higher Institute for Engineering, Computer Science and Management, New Cairo, Egypt. Tel: +20-1283320302*

[b]*Chemistry Department, College of Science, Imam Mohammad Ibn Saud Islamic University (IMSIU), Riyadh 11623, Saudi Arabia*

[c]*Center for Innovation and Entrepreneurship, Imam Mohammad Ibn Saud Islamic University (IMSIU), Riyadh 11623, Saudi Arabia*

[d]*Department of Chemistry, College of Science, Taif University, P.O. Box 11099, Taif 21944, Saudi Arabia*

[e]*Basic Science Department, Preparatory Year, University of Hail, Hail, Saudi Arabia*

[f]*Department of Chemistry, College of Science, King Faisal University, Al-Ahsa 31982, Saudi Arabia. E-mail: ekamoun@kfu.edu.sa; badawykamoun@yahoo.com*

[g]*Laboratory of Nano-Smart Materials for Science and Technology (LNSMST), Department of Physics, Faculty of Science, King Khalid University, PO Box 9004, Abha 61413, Saudi Arabia*

[h]*Nanotechnology Section, Egyptian Company for Carbon Materials, El-Sheraton/El-Nozha, Cairo 11757, Egypt*

1 Introduction

Advanced nanomaterials based on bismuth ferrite perovskite are attracting considerable attention because of their intriguing physics and possible uses in fields like spintronics and data storage microelectronics.[1] Due to the stereochemical activity of the Bi^{3+} ion electron pair, $BiFeO_3$ is a rhombohedral distorted perovskite with the space group $R3c$ and ferroelectric order ($T_C \sim 830$ °C). $BiFeO_3$ has a modulated cycloidal spin structure with a long periodicity of 62 nm and a G-type antiferromagnetic magnetic structure below $T_N = 370$ °C.[1] It was difficult for several researchers to synthesize pure $BiFeO_3$ since it is primarily contaminated with secondary phases such as Bi_2O_3 and $Bi_2Fe_4O_9$.[2–4] Additionally, single $BiFeO_3$ nanoparticles with divalent cations (Ba^{2+} and Ca^{2+}) replacing the trivalent cations of Bi^{3+} have exhibited weak ferromagnetism at room temperature.[5]

Bismuth is very volatile since it only has one pair of electrons. $BiFeO_3$'s commercial applications are limited due to its impurity and non-stoichiometry issues. Creating nanostructured materials that will cause the spin cycloid to break is one method to tackle these challenges, as long as the particle size is equal to the spin cycloid's, thus increasing the magnetism. Therefore, doping bismuth ferrite with different elements such as rare earth, alkaline earth metal, and transition metal in the A or B sites is another method to enhance its magneto-electric qualities.[6] Consequently, barium-doped bismuth ferrite nanostructures ($Bi_{0.9}Ba_{0.1}FeO_3$) were prepared by auto-combustion using different solvent approaches. To create such a material with the appropriate stoichiometry, porosity, and phase composition, specific methods such as hydrothermal,[7] sol–gel,[8] co-precipitation,[9] microwave irradiation, and solution-combustion have been reported previously.[10] These methods necessitate extensive processing stages, lengthy durations, and complex apparatus. Simple metal oxides, mixed oxides, ferrites, perovskites, spinels, garnets, nanophosphors, phosphates and hydroxy-phosphates, metals and metal–ceramic composites, microspheres, and metal sulfides are just a few of the fundamental kinds of nanostructures that can be produced using the appealing solution-combustion synthesis method with comparatively less time and effort.[11]

The lives of humans and other living things are in danger due to pollution, which has become a serious issue with the recent industrial development.[12] Several sources, including industrial discharge, sewage effluents, and agricultural industries, cause water contamination. Numerous dangerous and detrimental compounds, particularly organic pollutants like pesticides, antibiotics, and dyes, are present in contaminated water.[13] To verify the effectiveness of treatment and the environment's safety, it is also crucial to conduct a chemical analysis of the target pollutants and degradation products found in treated wastewater and industrial effluents. Therefore, further research is required to determine the toxicity and quality of the treated wastewater using toxicity tests.[14]

Dyes are colorful materials used in various industrial products, including paper, textiles, leather, furniture, and cosmetics.[15,16] Almost every industry uses dyestuffs to dye their products. Over 7×10^5 tons and approximately 10 000 different dyes and pigments are produced worldwide annually.[17] Approximately 10–15% of the dye is lost in the effluent during dyeing.[18] Azo dyes comprise 50–70% of all dyes and are the main family of synthetic aromatic dyes. Congo red (CR) is an asymmetric, sulfonated azo dye that is a member of the protein-binding dye class [1-naphthalenesulfonic acid, 3,3′-(4,4′-biphenylene bis(azo))bis(4-amino-)disodium salt]. The hue of CR solution depends on its pH. CR is an anionic bis azo dye known to metabolize human carcinogens such as benzidine.[19] The structural stability of these dyes makes them resistant to biodegradation due to which they are considered potential organic pollutants.[20]

Several methods have occasionally been used to exclude various dye types from effluents, including electrochemical coagulation, photocatalytic decolorization, electrochemical oxidation, adsorption, and microbiological degradation.[21–25]

Electrochemical methods have shown increased attention in wastewater cleanup throughout the last 10 years.[26] They fall into one of the following categories for dye removal: indirect electro-oxidation with powerful oxidants, electro-oxidation with active chlorine, electrocoagulation, electrochemical reduction, and electrochemical oxidation.[27] Since the electron, the primary reagent, is clean, these methods are environmentally friendly.[28] They have benefits, including low operating temperatures, easy operation, and basic equipment.[29] The high removal yields of contaminating chemicals with maximal energy resource management are noteworthy.[26] On the surface of the electrodes, the electric current causes redox reactions that change and destroy the organic component and nearly oxidize it completely to CO_2 and H_2O.[30]

0ferrite nanostructures can be created using various techniques, including chemical vapor deposition and precipitation,[31] electrochemical, microwave,[32] sol–gel,[33] Pechini method,[34] and combustion[35] Every technique has pros and cons of its own. When creating nanostructured $BiFeO_3$, it is important to regulate the shape of the nanoparticles. Pure $BiFeO_3$ synthesis has always been difficult since the final product is typically tainted with secondary phases like Bi_2O_3 and $Bi_2Fe_4O_9$.[36] Among these methods, auto-combustion methods are fast and easy, and this technique makes it feasible to manage the stoichiometry of chemical composition and dope different foreign atoms. An exothermic redox reaction between the precursor metal nitrates, regarded as an oxidant and a fuel, is essentially the solution-combustion synthesis. After all the water evaporates, the reactant mixture dehydrates into a gel and eventually self-ignites, either burning or smoldering. The reactants' self-combustion produces crystalline powder products with the appropriate stoichiometry.[37] The temperature of calcination,[38,39] the type and quantity of fuel (mixed or single),[39,40] the fuel-to-oxidizer ratio ($\varnothing$),[41] metal precursors,[42] and the reaction atmosphere, e.g. (air, N_2, Ar, and He)[43] all have a significant impact on the combusted product's crystallinity and particle size. Hence, in this study, $Bi_{0.9}Ba_{0.1}FeO_3$ has been successfully produced by combustion methods using dissimilar fuels such as glycine without solvent, glycine with solvent, urea, glucose, TEA, and EDTA. Because urea was said to be the best fuel for metal nitrates in solution combustion synthesis, some authors[34] favored it, while others preferred glycine and EDTA.[44–46] Few previous studies reported variables $\varnothing$ and examined some of their outcomes. In the beginning, Deshpande et al.,[47] focused on the effects of $\varnothing$ the fuel-nitrate system on iron oxide phase development and pore structure. In a few instances, they noticed the presence of several phases. Singh et al., Toniolo et al., and Ghosh used polyvinyl alcohol (PVA), urea, and glucose as the fuel with varying $\varnothing$, respectively.[48–50]

Additionally, Fathi et al.[36] found that iron oxide with $\varnothing = 1$ had two different phases in various oxides and that glycine was the fuel that produced the highest saturation magnetization. Conversely, fuel-deficient iron oxide ($\varnothing = 0.7$) had the maximum saturation magnetization, according to Wang et al.[51] A different author looked into how $\varnothing$ (0.0, 0.5, 1.0, and 1.5) affected the electrochemical energy storage characteristics and found that $\varnothing = 1.0$ performed the best. The magnetic and
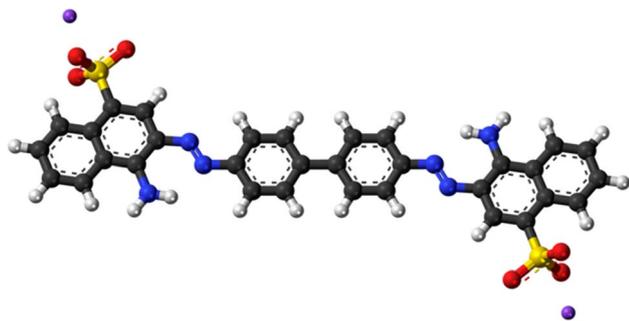
Fig. 1 Structure of Congo red dye.[52]

electric characteristics of BFO need to be improved for new electronic applications. Thus, examining this effect on the structure, electric and magnetic properties, and photocatalysis have been investigated and discussed in detail (Fig. 1).

To the best of our knowledge, we report here for the first time in the literature the formation of rhombohedral $Bi_{0.9}Ba_{0.1}FO_3$ in a good perovskite phase ratio by various fuels and the obtained hard ferromagnetic-like properties that are observed and studied in detail. Moreover, Ba^{2+} dopant ions were chosen to replace trivalent Bi^{3+} cations in $BiFeO_3$ with another divalent cation. For example, Ba^{2+} is expected to change the electrical and magnetic properties by reducing valence fluctuations in Bi^{3+}. Previous research indicates that most published reports primarily examined the impact of differences $\varnothing$. However, few studies have addressed the combustion technique of synthesis with various fuels and have not provided a thorough examination. Thus, in this study, we intend to examine the structural, electric, magnetic, and photocatalytic characteristics of $Bi_{0.9}Ba_{0.1}FeO_3$ synthesized by a solution-combustion approach with fixed $\varnothing = 1$.
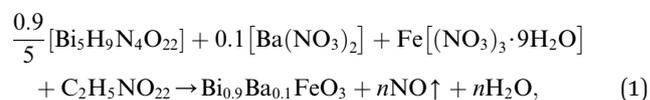
2 Materials and methods

2.1. Material

Bismuth subnitrate $Bi_5H_9N_4O_{22}$, barium nitrate $Ba(NO_3)_2$, iron nitrate $Fe(NO_3)_3 \cdot 9H_2O$, glycine $C_2H_5NO_2$, urea CON_2H_4, triethanolamine (TEA) $C_6H_{15}NO_3$, ethylene diamine tetraacetic acid (EDTA) $C_{10}H_{16}N_2O_8$, glucose $C_6H_{12}O_6$, ammonium hydroxide NH_4OH, distilled water, Congo red dye $C_{32}H_{22}N_6Na_2O_6S_2$, ascorbic acid $C_6H_8O_6$, isopropyl alcohol C_3H_8O, nitric acid HNO_3, and sodium nitrate $NaNO_3$ were obtained from Sigma-Aldrich, Germany; all used chemicals were analytical-grade chemicals.

2.2. Synthesis of $Bi_{0.9}Ba_{0.1}FeO_3$ nanocomposites

Nano-sized $Bi_{0.9}Ba_{0.1}FeO_3$ powders have been synthesized by the combustion route; bismuth subnitrate, barium nitrate, and iron nitrate are mixed with an amount of fuel. Stoichiometric amounts of $Bi_5H_9N_4O_{22}$, $Ba(NO_3)_2$, $Fe(NO_3)_3 \cdot 9H_2O$ were dissolved separately in distilled water to form the nitrate solutions (except Bismuth subnitrate, which was dissolved in a small amount of dilute nitric acid with distilled water). All solutions were mixed in one beaker and put on magnetic stirring at 600 rpm. The required amount of fuel glycine, urea, TEA, $C_6H_{15}NO_3$, EDTA, and glucose with a molar ratio determined according to the oxidation/reduction number of reactants in eqn (1), represented in Table 1, was added to the nitrates solution to form the precursor solution for $Bi_{0.9}Ba_{0.1}FeO_3$ composition according to eqn (2). MI : TEA = 1 : 4, there is no need to adjust the pH for glycine, urea, and TEA. A molar ratio (MI : EDTA) = (2 : 1), the amount of EDTA is dissolved in distilled water with the addition of NH_4OH until it reached a pH of 8–10. The nitrate solution was added dropwise to the EDTA solution to prevent an irreversible reaction. Glucose (12 g) was dissolved in 100 mL distilled water and added to the nitrate solution, keeping pH = 7 by carefully adding NH_4OH. The precursor solution was heated on a hot plate with magnetic stirring at 600 rpm at 90 °C for 10 h, and the water gradually vaporized during heating and formed a transparent viscous gel. The flow chart is shown in Fig. 2(a).

For instance, glycine (5.4495 g) was used as fuel with and without solvent, as revealed in eqn (1).

$$\frac{0.9}{5}[Bi_5H_9N_4O_{22}] + 0.1[Ba(NO_3)_2] + Fe[(NO_3)_3 \cdot 9H_2O]$$
$$+ C_2H_5NO_{22} \rightarrow Bi_{0.9}Ba_{0.1}FeO_3 + nNO\uparrow + nH_2O, \quad (1)$$

$$\frac{0.9}{5}[-20] + 0.1[-10] + 1[-15] = n[+9], \ 0.653 = nF. \quad (2)$$

Table 1 Structure parameters of $Bi_{0.9}Ba_{0.1}FeO_3$ NPs

| Parameter	EDTA	Glucose	Glycine	TEA	Urea	Without
Chemical formula	$C_{10}H_{16}N_2O_8$	$C_6H_{12}O_6$	$C_2H_5NO_2$	$C_6H_{15}NO_3$	CON_2H_4	$C_2H_5NO_2$
Reduction no.	40	24	9	33	6	9
T (combustion), °C	280 flaming	200 flaming	180 smoldering	180 smoldering	250 smoldering	280 smoldering
% Perovskite phase	100	100	100	74	83	78
a, Å	3.9677	3.9337	3.9526	3.9503	3.9468	3.9783
C, Å	15.8311	15.7995	15.5289	15.8979	15.8563	15.4559
V, Å³	249.2237	244.4821	242.6094	248.0859	246.9972	244.6185
Cs, nm	26.66	23.96	23.78	18.55	18.52	27.66
W–H, nm	23.83	23.83	23.83	34.29	23.83	34.29
Grain size, nm	79.74	90.13	292.8	104.18	56.4	53.77
Dislocation $\times 10^{-3}$, nm^{-2}	1.40	1.76	1.76	2.9	2.9	1.3
Strain $\varepsilon \times 10^{-3}$	6.15	5.2	6	7.03	7.47	5.22
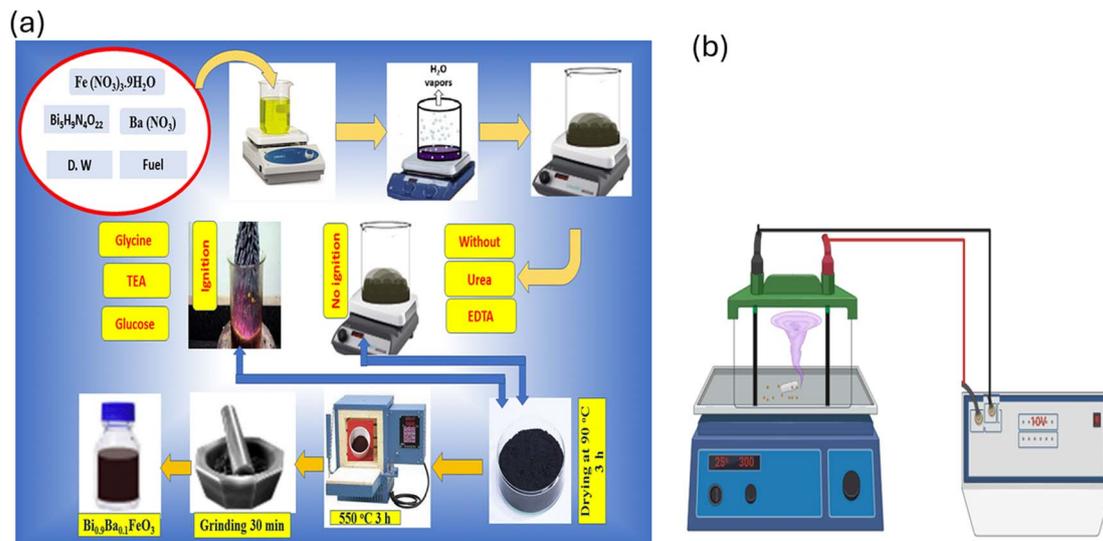
Fig. 2 (a) Scheme of the co-precipitation processes of the nano-$Bi_{0.9}Ba_{0.1}FeO_3$ and (b) electrochemical system for degradation of CR dye.

The total oxidizing and reducing valences of the fuel (F) and oxidizer (O) were used to calculate the stoichiometry of the redox mixture for combustion. This allowed the equivalency ratio, or Φe (O/F), to reach unity and generate the maximum amount of heat. The glycine-to-nitrate ratio (GNR) was calculated based on the oxidizing and reducing valences of nitrates and glycine, respectively. The oxidizing valence of bismuth subnitrate is as follows:

$$[Bi_5H_9N_4O_{22} = 5 \times 3 + 9 \times 1 + 4 \times 0 + (-2 \times 22) = -20],$$
$$[Ba(NO_3)_2 = 1 \times 2 + 0 \times 2 + (-2 \times 6) = -10] \text{ and}$$
$$[Fe(NO_3)_3 = 1 \times 3 + 0 \times 3 + (-2 \times 9) = -15],$$

where the oxidizing valence of water is $H_2O = 0$, and the reducing valence of glycine is $[C_2H_5NO_2 = 2 \times 4 + 1 \times 5 + 0 \times 1 + (-2 \times 2) = 9]$.

Thus, the total values of all nitrates should be balanced by the reducing valences of the fuel glycine. Therefore, eqn (2) states that n moles of fuel are needed to achieve the stoichiometric composition of the redox mixture, where n is the number of moles of fuel needed to release the most energy, and F is the total valences of fuel (equal to 9). Therefore, the appropriate moles of glycine, as shown in Table 1, are necessary for the stoichiometric composition of the redox mixture. Based on the abovementioned computation, stoichiometric reactant amounts were combined in an agate mortar and pestle. Because metal nitrates are hygroscopic, a slurry was created. A large, smoldering, fluffy product was produced in the beaker because the combustion process began with the slurry being dried at 80 °C and then heated to 150 °C.

2.3. Electrocatalytic measurements

A two-electrode electrochemical cell with a DC power supply voltage of 10 volts was used for the electrochemical reaction. Two electrodes were made of graphite, and 0.01 g of $Bi_{0.9}$-$Ba_{0.1}FeO_3$ catalyst was added to 200 mL of an aqueous solution

of Congo red (CR: 10 ppm) dye before 10 mL of 1 M NaCl was added. An electrocatalytic technique was used to break down the CR dye in suspensions before they were exposed to radiation for 30 min, as shown in Fig. 2(b). The electrodes were spaced 2 cm apart. A UV-vis spectrophotometer measured the CR dye maximum absorption peak spectra in 3 mL of solution at various time points. The degradation percentage was evaluated using eqn (3).[53]

$$\text{Degradation } \% = \frac{A_0 - A}{A_0} \times 100 \qquad (3)$$

As a result, eqn (4) can be used to obtain the kinetic constant.

$$\ln\left(\frac{A}{A_0}\right) = -Kt \qquad (4)$$

where A_0, A, and K represent the initial absorbance, the absorbance at the time points during the degradation process, and the kinetic constant (min^{-1}), respectively.

2.4. Devices and instrumental characterization

Phase identification and structure analysis of samples were investigated by XRD (Bruker, Germany) with $CuK_{\alpha 1}$ radiation ($\lambda = 1.5405$ Å), and the step scan mode 2θ ranging from 10–80°, with a step size of 0.02°. XRD peaks were indexed using the X'pert High Score software program and Rietveld refinement software programs. FTIR (PerkinElmer Spectrum, Germany) spectroscopy was used to identify the functional groups in the ν 400–4000 cm^{-1} wavenumber range in the as-synthesized samples. The morphological and elemental analyses of synthesized samples were examined using SEM (JEOL JSM-6390, Japan), close-fitting with an energy dispersive spectroscopy (EDS) at a voltage of 15 kV and with different resolutions of 10 μm and 300 nm. The average particle size was calculated by using ImageJ software program. To perform DC measurements, the powder was pressed at 250 bars in a pellet shape with a 13 mm diameter and 2 mm thickness. A KEITHLEY cell

station (616 digital electrometer, Germany) was used to measure the DC conductivity of prepared samples and DC electrical conductivity. A homemade electrometer device with a temperature range of ambient temperature to 150 °C in steps of 5 °C was used to measure the temperature dependency of the samples' DC conductivity. Before measurements, in the specifically made holder made of brass and Teflon as a two-probe contact, two copper plates were positioned between the samples as an ohmic contact. The vibrating sample magnetometer, VSM (Lake Shore-7410, Germany), was used to measure the magnetizations of all samples at room temperature within the magnetic field range of ±20 kOe.

3 Result and discussion

3.1. XRD analysis

As shown in Fig. 3(a), the creation of a single-phase distorted tetragonal structure was demonstrated by the produced nanocomposites' XRD pattern with standard data (JCPDS #01-089-8414), which is described in the $P4/mmm$ space group. The increase of Ba doping in such a composition transforms that structure to a cubic structure, whereas $Bi_{0.9}Ba_{0.05}Sm_{0.05}FeO_3$ nanocrystalline film has demonstrated a pure rhombohedral crystal structure, where $BiFeO_3$, $Bi_{0.9}Ba_{0.1}FeO_3$, and $Bi_{0.9}Sm_{0.1}$-FeO_3 films displayed a polycrystalline distorted rhombohedral crystal structure and belong to the $R3c$ space group.[54,55] The shift is caused by a minor difference in the atomic radii, and the indicated peaks of $Bi_{0.9}Ba_{0.1}FeO_3$ correspond. The tiny change in the crystalline size of the nanocomposites is caused by the size difference in the ionic radius of the Bi^{3+}, Ba^{2+}, and Fe^{3+} ions linked to the compressive strain produced in the crystal matrix. The high-intensity peak of (014) at 31.9° appears as an overlapped single peak rather than peak splitting at I_{max}, as is frequently observed in BFO nanoparticles, as shown in Fig. 3(a). It is noteworthy that the multiferroic samples exhibit a discernible drop in the intensity of the (014) peak, which could be caused by strain and the difference in atomic radii. This may impact the ferromagnetic and ferroelectric characteristics of BFO and doped BFO systems, particularly their functional behavior. Scherer's equation determined the crystallographic size based on the most noticeable peak at $2\theta = 31.9°$. According to eqn (5), the crystallite size (D) was calculated using the Debye–Scherrer formula:[56]

$$D = \frac{k\lambda}{\beta_D \cos\theta}, \tag{5}$$

where λ is the incident radiation wavelength (1.5415 Å), β_D is the full-width half-maximum in radians, θ is the angle of diffraction, and D is the crystallite size of the most intense peak. The Scherrer equation yields a crystallite size from 26.66 to 18.52 nm, as shown in Fig. 3(d). XRD determines additional parameters, $e.g.$, the microstrain (ε) and the dislocation density (δ). Table 1 displays the unit cell's volume and lattice characteristics. The Williamson–Hall equation in eqn (6) is used to calculate the size of crystallites:

$$\beta_{hkl}\cos\theta = \frac{k\lambda}{D} + 4\varepsilon, \tag{6}$$

The dislocation density, using the square of the reciprocal of the crystallite size, was calculated using eqn (7).[57]
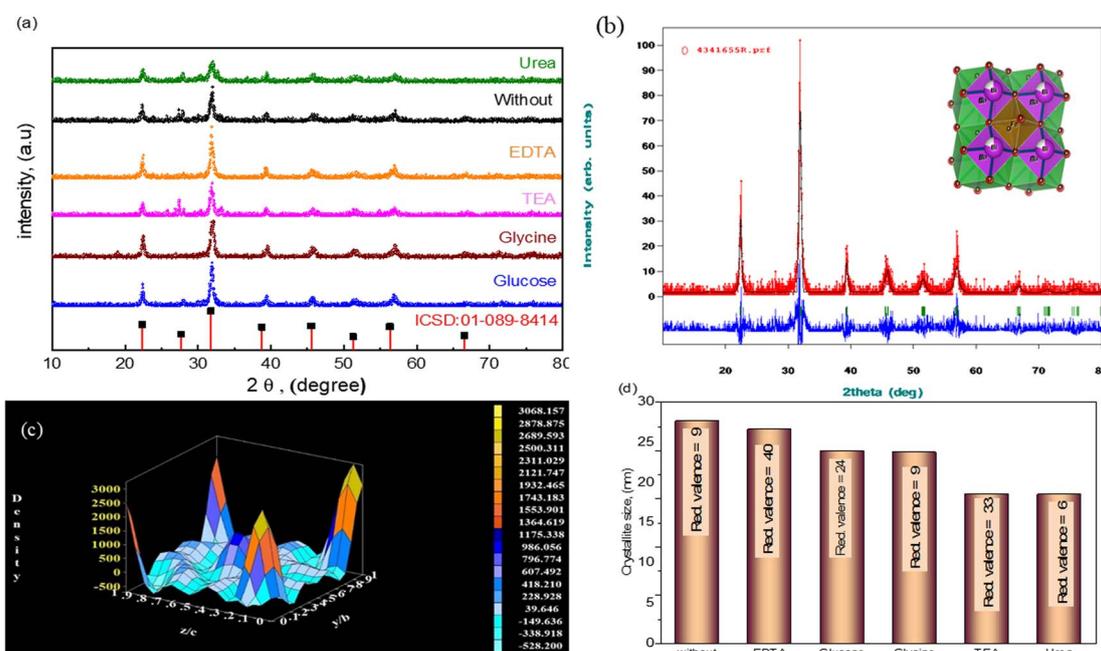
$$\delta = \frac{1}{D^2}, \tag{7}$$

Fig. 3 (a) XRD data of the $Bi_{0.9}Ba_{0.1}FeO_3$ nanoparticles with different fuels, (b) Rietveld refinement using FullProf software of $Bi_{0.9}Ba_{0.1}FeO_3$ nanoparticles, (c) X-ray electron density, and (d) crystallite size $vs.$ solvent.

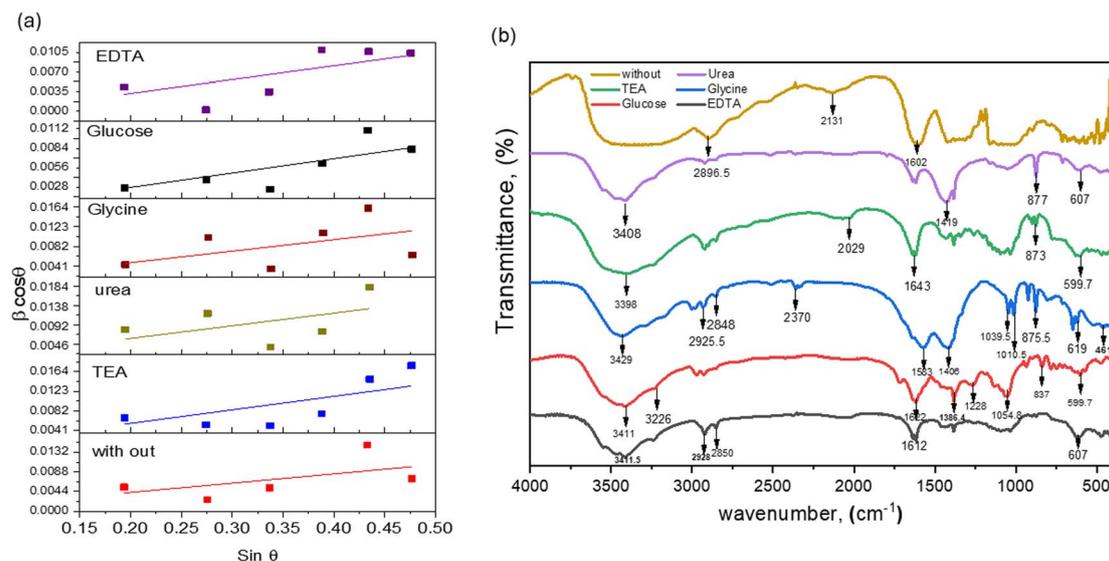**Fig. 4** (a) W–H for $Bi_{0.9}Ba_{0.1}FeO_3$ with different fuels and (b) FTIR spectra of $Bi_{0.9}Ba_{0.1}FeO_3$ with different fuels.

The grasped microstrain is shown by the slope of the line (slope = 4ε), as shown in Fig. 4(a). The clear intersection of the line with the vertical y-axis confirms the crystallite size. This relationship, known as the Williamson–Hall relation, exists between β cos θ and sin θ [24]. The tolerance factor of $Bi_{0.9}Ba_{0.1}FeO_3$'s unit cell calculations shows that it agrees well with the material's average crystalline size. Nonetheless, it was observed that several composites had a trace quantity of the $Bi_{24}Fe_2O_{39}$ and Bi_2O_4 impurity phases. $Bi_{0.9}Ba_{0.1}FeO_3$'s lattice parameters are similar to those in literature.[36] Ba–O = 2.854 Å, Bi–O = 2.426 Å, and Fe–O = 2.028 Å are the bond lengths and atomic locations of different atoms taken from the Rietveld

refinement of XRD data. Fig. 3(b) displays the crystal structures of $Bi_{0.9}Ba_{0.1}FeO_3$ nanoparticles as determined by VESTA software. Fe atoms or cations are found at site 3b, Ba- and Bi-atoms or ions are found at site 3a, and oxygen is found at site 9e of the Wyckoff position. Six oxygen atoms encircle iron (Fe-) to create the octahedral structure of FeO_6. The electrons in Fig. 3(d) have the same units as the F(H) per volume Fourier complex. Furthermore, many electrons are present at the same iron atomic site based on the electron distribution inside the unit cell. The electron density map inside our sample's unit cell is similar to the compound of $Nd_{0.5}Ba_{0.5}FeO_3$.[58]
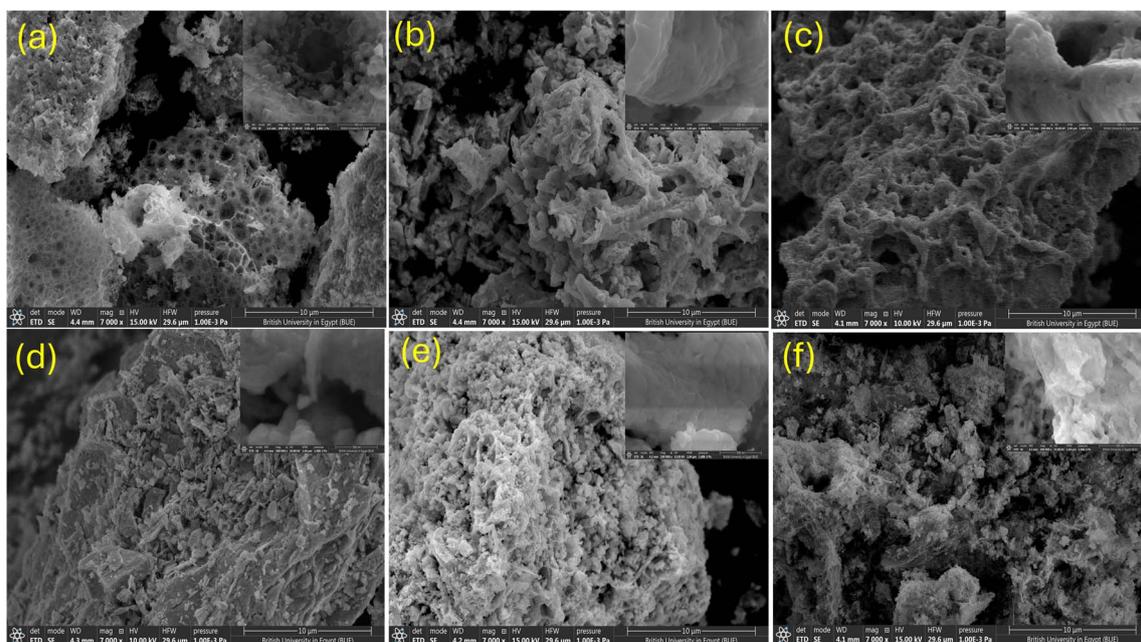

Fig. 5 SEM of $Bi_{0.9}Ba_{0.1}FeO_3$ at 10 micro-magnifications with different fuels: (a) EDTA, (b) glycine, (c) glucose, (d) urea, (e) TEA, and (f) without-fuel.

3.2. FTIR analysis

The FTIR spectra of $Bi_{0.9}Ba_{0.1}FeO_3$, synthesized using the combustion method using different fuels, are shown in Fig. 4(b). The weak bands around ν 600 and 850 cm^{-1} are associated with the vibrational modes of the metal–oxygen bond: Fe–O stretching and the symmetric Bi/Ba–O/Fe–O vibrations in the BiBaFeO$_3$ units, respectively.[59] The stretching mode of the C–O bond is associated with the band at ν 1058 cm^{-1}.[59] As is well known, the chemisorption of ambient carbon dioxide results in the production of the carbonate group, which is represented by the band at ν 1406 cm^{-1}.[59] In certain compositions, the peak at ν 1372 cm^{-1} is assigned to the strong vibration of the NO_3^- group. The peaks corresponding to the C–H stretching modes appear at ν 2920 cm^{-1}. The hydroxyl groups at the low-coordination sites or faults cause the wide band at ν 3400 cm^{-1}.[59] However, doping with Ba ions broadens the band and the aforementioned functional groups of $Bi_{0.9}Ba_{0.1}FeO_3$ (ν 522, 844, and 1365 cm^{-1}, respectively).

3.3. SEM investigation

The nanostructure/morphology and elemental concentrations of $Bi_{0.9}Ba_{0.1}FeO_3$ were determined using SEM/EDS investigations. Fig. 5 displays SEM micrographs of the synthesized nanomaterials. $Bi_{0.9}Ba_{0.1}FeO_3$ nanoparticles' uneven morphology with aggregation was visible in the SEM images. For these tiny particles, the comparatively high magnetism caused the agglomerated particles to form. The high surface energy of the produced nanoparticles is thought to cause agglomeration. Due to doping and size reduction of the composites, this results in the unit-cell disorder. Herein, various $Bi_{0.9}Ba_{0.1}FeO_3$ morphologies, including spongy structures with numerous cavities, coral-like, sheet-like, and rod-like forms, were synthesized using solvents such as EDTA, glucose-glycine, TEA, urea, and without any solvent, respectively. Such trends prove that the morphology of our

samples depends not only on the synthesis method but also on the type of solvent used. Furthermore, the two combustion approaches, flaming or smoldering, affect the grain growth size, where the medium grain size forms in the flaming case. By contrast, the smoldering case creates agglomerated grain at low temperatures <200 °C and small grain at high temperatures >250 °C, as listed in Table 1.

The energy dispersive spectrum (EDS) of $Bi_{0.9}Ba_{0.1}FeO_3$ nanocomposites was presented in Fig. 6. It confirmed the presence of Bi, Ba, Fe, and O in our samples. No foreign elements in $Bi_{0.9}Ba_{0.1}FeO_3$ were observed in Fig. 6. The agglomeration process and variety in grain morphologies are caused by irregular or discontinuous grain development, where some grains expand more quickly than others as the sintering temperature rises because many solvents are present.

3.4. DC conductivity measurements

The variation in DC conductivity (σ_{DC}) of multiferroic nanoparticles as a function of absolute temperature is typical and shows an inverse relationship, as displayed in Fig. 7(a and b). Up to a crucial temperature $D/2$ (D: Debye temperature), a linear temperature dependency is evident.[60] The DC conductivity then obeys the Arrhenius relation eqn (8), as the slope varies with divergence from linearity, and the activation energy is temperature-dependent. The DC electrical conductivity for samples was calculated according to the well-known Arrhenius equation as follows.[61,62]

$$\sigma_{DC} = \sigma_o e^{-E_a/K_B T}, \quad (8)$$

where σ_o is the pre-exponential factor, E_a is the activation energy in eV for electrical conductivity, K_B is the Boltzmann's constant $K_B = 8.6 \times 10^{-5}$ eV K^{-1}, and T is the absolute temperature. The activation energy was calculated to be 0.39, 0.38, 0.30, 0.18, 0.16, and 0.075 eV for EDTA, glycine, urea, without, TEA, and glucose,
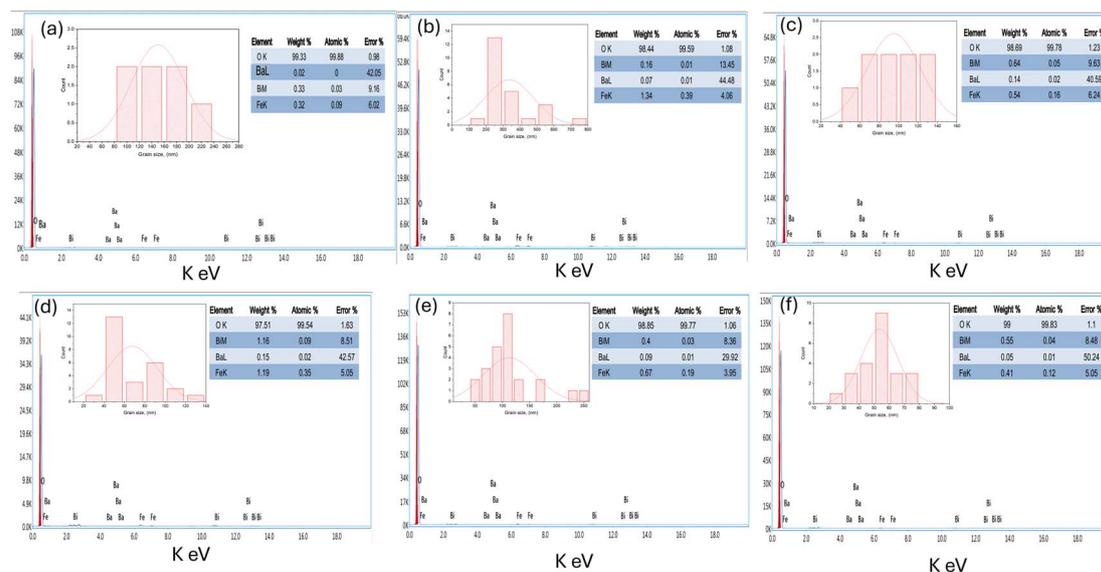

Fig. 6 EDX and percentage of elements, and histogram of particle size of $Bi_{0.9}Ba_{0.1}FeO_3$ NPs with different fuels: (a) EDTA, (b) glycine, (c) glucose, (d) urea, (e) TEA, and (f) without-fuel.
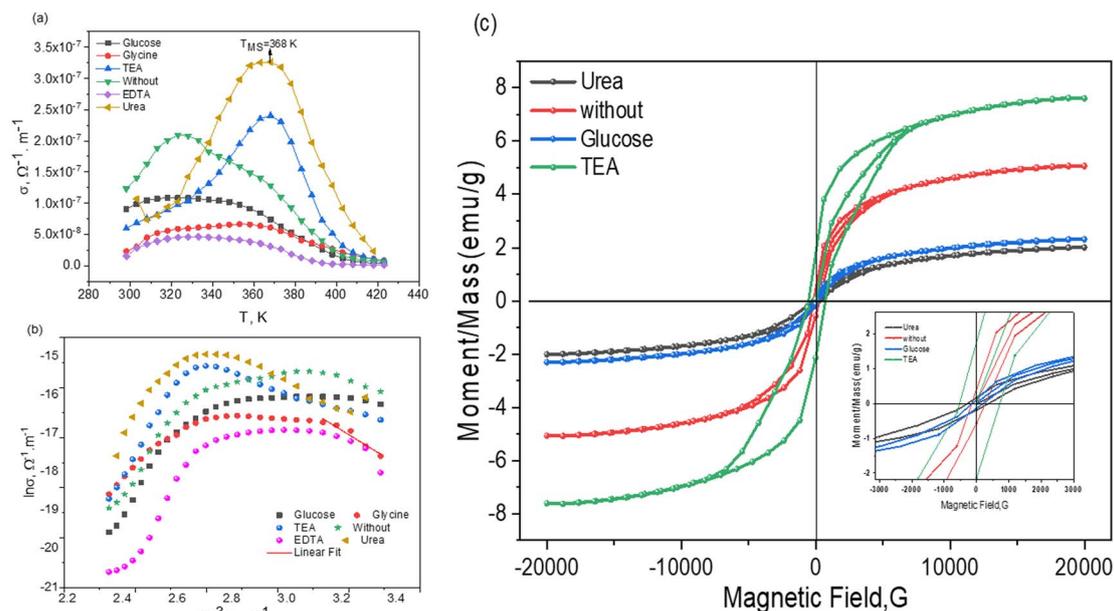
Fig. 7 (a and b) DC conductivity dependence on temperature and (c) magnetization *vs.* magnetic field at room temperature for $Bi_{0.9}Ba_{0.1}FeO_3$ NPs with different fuels.

respectively. At high temperatures, conductivity is generated by a thermionic emission process in which carriers possess enough energy to cross the potential barrier. It is obvious that σ_{dc} increases with temperature, indicating the samples' semi-conducting nature. Additionally, a transition temperature of 368 K was observed. This temperature shifted to lower values for other fuels. The reduction in crystallite size may contribute to the increased conductivity. However, grain boundary scattering affects the electrical conductivity. These grain boundaries serve as traps, ensnaring electrons and creating a potential barrier. Conduction electrons scatter when this barrier is present at the grain boundaries, reducing conductivity. Therefore, the observed increase in conductivity can be attributed to the reduced grain boundary scattering[63] caused by the smaller crystallite size.[60]

3.5. VSM measurement

We used a vibrating sample magnetometer (VSM) to examine the magnetic order of the prepared bismuth ferrite samples at

ambient temperature. Notably, significant hysteresis was observed for every sample, with limited values of the coercive field, remnant magnetization, and saturation magnetization, which are listed in Table 2. Fig. 7(b) displays the M(H) loop for $Bi_{0.9}Ba_{0.1}FeO_3$ ferrite at 300 K. Weak ferromagnetic order was also observed for urea and glucose samples; however, clear ferromagnetic behavior was observed for no-fuel and TEA samples. All samples reach magnetization saturation below 20 kOe magnetic field. Due to their grain size constriction, which has been reported to partially disrupt the long-range spiral spin structure of bulk BFO,[64] $Bi_{0.9}Ba_{0.1}FeO_3$ nanostructures with typical dimensions below 62 nm can exhibit advantageous magnetic characteristics.

The value of saturation magnetization, M_s, comes out to be 2.01, 2.30, 5.06, and 7.62 emu g^{-1} for urea, glucose, no-fuel, and TEA, respectively, which is greater than the same composition value 0.31 emu g^{-1}.[64] Different shape anisotropy, magneto-crystalline anisotropy, and varying degrees of defects in the

Table 2 Crystallite size D, saturation magnetization M_s, coercivity H_c, remanent magnetization M_r, and sequence of Ba-doped bismuth ferrites at room temperature

Methods	M_s, emu g^{-1}	H_c, (Oe)	Mr	Seq. $\times 10^{-3}$	Ref.
Without solvent	5.0698	210.29	0.4923	97	Present work
TEA	7.6241	623.09	1.9590	257	
Glucose	2.3050	168.87	0.1262	55	
Urea	2.0105	325.30	0.1799	89	
$Bi_{0.9}Ba_{0.1}FeO_3$, co-precipitation	1.46	50	—	—	54
$Bi_{0.9}Ba_{0.1}FeO_3$, solid-state reaction	0.12	907 Oe	—	—	68
$Bi_{0.9}Ba_{0.1}FeO_3$, sono-chemical technique	0.31 (at 8 kOe)	1918	0.04	—	64
$Bi_{0.9}Ba_{0.1}FeO_3$, hydrothermal	7.24 (at 16 kOe)	2240	—	—	64
$Bi_{0.9}Ba_{0.1}FeO_3$, co-precipitation	1.46	50	—	—	64
$Bi_{0.9}Ba_{0.05}Sm_{0.05}FeO_3$, Co-precipitation	0.15	200	—	—	64

different nanoforms could cause this variation in M_s magnitude for our samples. The hysteresis loop's crossings with the vertical magnetization axis allow for extracting the remanence magnitude M_r. The coercivity field, H_c, can reflect the coercivity of a ferromagnet or ferrimagnet. The magnetic field intensity needed to bring the magnetic sample's magnetization down to zero once saturation has been attained is denoted by the value of H_c. The Hc values obtained for our samples (623.09–168.87 Oe) are significantly higher than those reported in the literature. TEA sample has the greatest values of M_S (7.63 emu g^{-1}), M_r (1.96 emu g^{-1}), and coercive field H_c (623.09 Oe). This might be because their samples contain a secondary phase while others do not. As seen in the Table 2, magnetic properties, including coercive field, remnant magnetization, and saturation magnetization values, are similar to those previously reported in the literature.[65] Since the ionic size of barium (1.42 Å) is larger than that of bismuth (1.03 Å), the variation in magnetic parameters for the same composition may be attributable to the incorporation (which greatly depends on the type of fuel) of Ba^{3+} in BFO may result in a significant off-center movement of Fe^{3+} ions in the octahedral.[66] This kind of variation causes the perovskite structure to be distorted by doping, which results in a smaller Fe^{3+}–O–Fe^{3+} bond angle and less antiferromagnetic interaction. As a result, the magnetization of Bi$_{0.9}$Ba$_{0.1}$FeO$_3$ is significantly altered. Furthermore, barium has a valency of +2, while bismuth has a valency of +3. Therefore, charge compensation will be required for incorporating barium into the bismuth site. As a result, Fe^{4+} or oxygen vacancies may occur; the former may statistically distribute with Fe^{3+} in the octahedron in BBFO, resulting in ferromagnetism and net magnetization.[67] Furthermore, BiFeO$_3$ has a spiral spin magnetic structure with a period of 62 nm. Consequently, Bi$_{0.9}$Ba$_{0.1}$FeO$_3$ nanograins that aggregate into ~292 nm particles may fragment into grains that aggregate into ~53 nm particles, resulting in improved magnetic properties.[66]

3.6. Electrocatalytic degradation of CR dye

The electrocatalytic activity of the prepared Bi$_{0.9}$Ba$_{0.1}$FeO$_3$ samples was analyzed by studying the electro-degradation of CR dye (10 ppm) in aqueous solutions at constant voltage and at different time points. The absorption spectra of CR dye in aqueous solutions show an absorption band at 494 nm. These spectra were first recorded in the presence of electrocatalysts and at different irradiation times. However, when Bi$_{0.9}$Ba$_{0.1}$FeO$_3$-based electrocatalysts are present, clear dye-degradation effects are visible. It is expected that the fuel type will have a significant impact on the catalytic activity of the nanoparticles, as shown by the absorption spectra for CR dye solutions in Fig. 8. The produced nanoparticles were utilized as a catalyst in the electrocatalytic oxidation process of CR dye, which was exposed to a constant voltage for up to 4 min, to examine the effects on the catalytic performance of the product particles from the reagent material used as fuel in the synthesis of Bi$_{0.9}$Ba$_{0.1}$FeO$_3$ nanoparticles. The absorption band's intensity decreased as the irradiation period increased. Furthermore, compared to the solvent-free condition, the declining tendency was stronger for the solvent catalysts (Bi$_{0.9}$Ba$_{0.1}$FeO$_3$). The breakdown of azo bonds in organic dyes demonstrates the synergistic effect of Fe- and Bi.[69]

The effect of fuels on the structural and electrocatalytic properties of Bi$_{0.9}$Ba$_{0.1}$FeO$_3$ NPs using glycine as a green fuel is investigated. The degradation of CR dye is shown in Fig. 9(a). Bi$_{0.9}$Ba$_{0.1}$FeO$_3$ NPs achieved 67.4% degradation without fuel; similarly, the degradation increased up to 96.5% within 4 min in the presence of glycine, which is ascribed to its large grain size. The kinetics data are presented in Table 3. The determined rate constant of Bi$_{0.9}$Ba$_{0.1}$FeO$_3$ NPs using glycine was 0.82486 min^{-1}, which was four times higher than that for the sample prepared without fuel. Table 3 displays the regression correlation coefficient (R^2) values, which were determined and
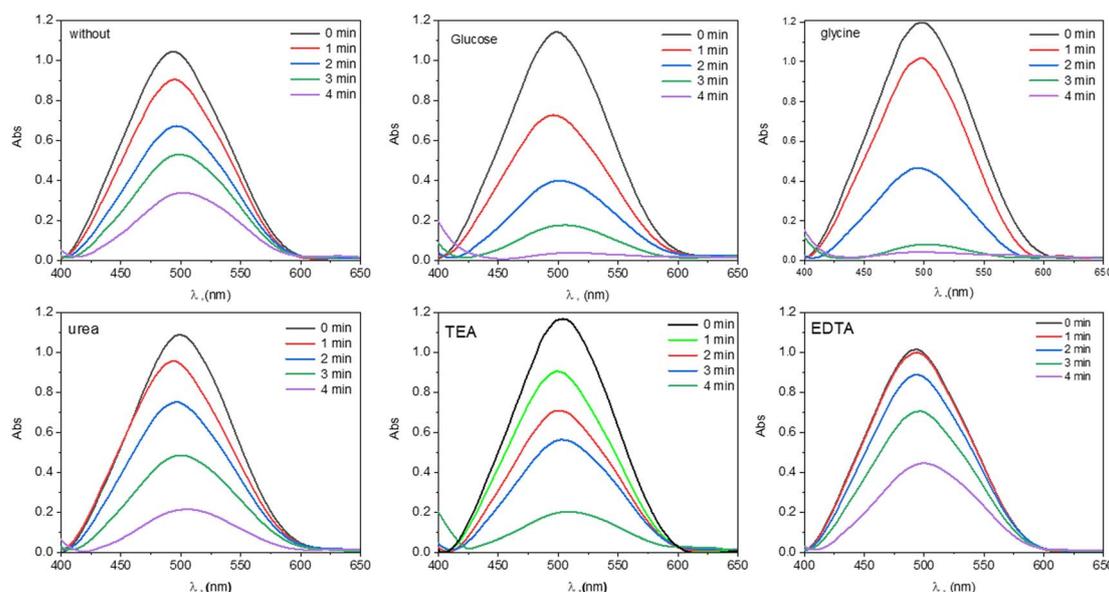

Fig. 8 Absorption spectra of CR dye solutions under Bi$_{0.9}$Ba$_{0.1}$FeO$_3$ NPs in different fuels.

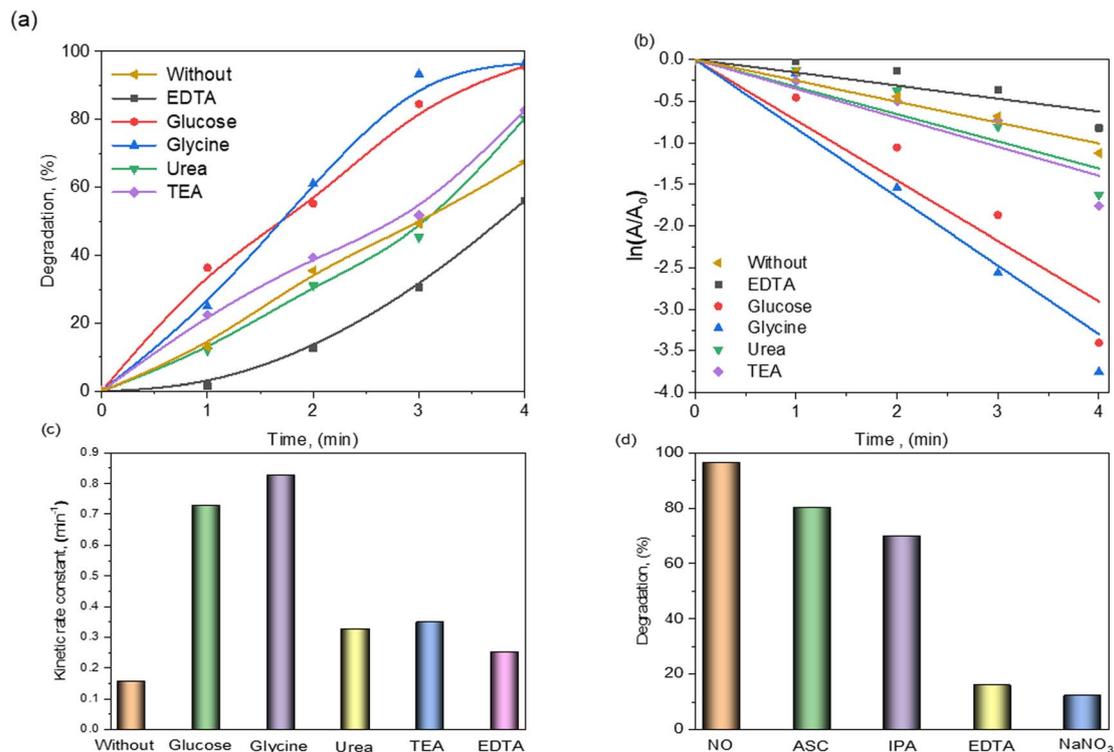© 2025 The Author(s). Published by the Royal Society of Chemistry

Fig. 9 (a) Electro-degradation of CR dye against reaction time, (b) reaction rate, (c) variation of the kinetic coefficient of the electrocatalysis reaction, and (d) effect of radical scavengers on the electrocatalytic degradation of CR dye.

Table 3 Calculated degradation, pseudo-first-order rate constant (k), and regression correlation coefficient (R^2)

Sample	Degradation (%)	Kinetic rate (min^{-1})	R^2
EDTA	56.03	0.15552	0.90782
Glucose	95.67	0.72607	0.96483
Glycine	96.50	0.82486	0.94641
Urea	80.34	0.34854	0.92737
TEA	82.68	0.01973	0.92938
No fuel	67.48	0.25147	0.98126

ranged between 0.90 and 0.98. As seen from the R^2 values, the reasonably excellent linear fits suggest that electro-degradation proceeds according to pseudo-first-order kinetics, as illustrated in Fig. 9(b and c). $Bi_{0.9}Ba_{0.1}FeO_3$ NPs with glycine have a considerably smaller particle size compared with $Bi_{0.9}Ba_{0.1}$-FeO_3 particles without fuel and have significantly higher electrocatalytic activity. This is attributed to the available active sites on the particle's surface.

3.7. Influence of radical scavengers on electrocatalytic activity

Reactive species trapping studies are necessary to determine the mechanism underlying the high electrocatalytic activity of $Bi_{0.9}Ba_{0.1}FeO_3$ electrocatalysts. The degradation (%) of CR dye in the presence of glycine of $Bi_{0.9}Ba_{0.1}FeO_3$ NPs with EC was investigated using radical scavengers. Ascorbic acid (ASC),

isopropyl alcohol (IPA), sodium nitrate $NaNO_3$, and EDTA were used as scavengers of $O_2^{-\bullet}$, $^\bullet OH$, e^-, and h^+ in these assays.[70] When CR dye was electrocatalytically broken down with EDTA present, the degradation efficiency dropped slightly from 96.5% to 15.9%, as illustrated in Fig. 9(d). Nevertheless, the degradation efficiency further decreased from 96.5% to 12.1% by adding $NaNO_3$. This result indicates that the degradation of CR dye is caused by h^+ and e^-.

3.8. Electro-oxidation mechanism of CR

The overall catalysis of organic dye depends on its degradation in the presence of an electrocatalyst. The following method adds sodium chloride to CR dye during indirect electro-oxidation to improve conductivity, leading to the formation of hypochlorite ions.[71]

$$\text{Anode: } 2Cl^- \rightarrow Cl_2 + 2e^- \tag{9}$$

$$\text{Cathode: } 2H_2O + 2e^- \rightarrow H_2 + 2OH^- \tag{10}$$
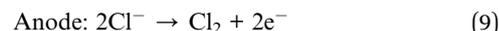
The Cl_2 hydrolysis in the solution occurs following the subsequent reaction:

$$Cl_2 + H_2O \leftrightarrow HOCl + H^+ + Cl^- \tag{11}$$
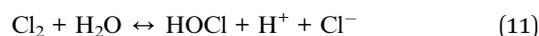
and further dissociates generating a hypochlorite ion.

$$HOCl \leftrightarrow H^+ + OCl^- \tag{12}$$
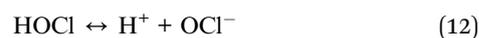
In the electrocatalytic breakdown of CR dye effluent by chlorine production, the hypochlorite ions act as the primary oxidizing agent in pollutant degradation.

$$CR\ dye + OCl^- \leftrightarrow CO_2 + H_2O + Cl^- \tag{13}$$
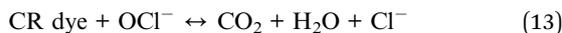
The valence band (VB) holes are produced when electrons from the valence band (VB) are driven into the conduction band after following an electric path longer than the band gap energy E_g of $Bi_{0.9}Ba_{0.1}FeO_3$ NPs. Electrons travel through the external circuit to counter electrochemical potential during degradation, creating highly reactive superoxide anion radicals (O_2).

$$e^- + O_2 \rightarrow O_2^- \tag{14}$$

$$h^+ + H_2O \rightarrow OH^\cdot \tag{15}$$

$$CR\ dye + OCl^- + OH^\cdot \rightarrow CO_2^\cdot + ^\cdot H_2O + Cl^- \tag{16}$$

4 Conclusions

In the present work, the synthesis of $Bi_{0.9}Ba_{0.1}FeO_3$ nanostructures using different fuels was achieved using the auto-combustion method. XRD reveals single-phase $Bi_{0.9}Ba_{0.1}FeO_3$ nanomaterials alongside a small number of secondary phases. The R3C space group for the rhombohedral structure was assigned to samples with crystallite size ranging from 18.22 to 27 nm. SEM reveals that the grain size ranged from 56 to 292 nm. The change in magnetic behavior is due to the presence of smaller-sized nanoparticles. The highest values of M_S (7.63 emu g^{-1}), M_r (1.96 emu g^{-1}), and coercive field H_c (623.09 Oe) were observed in the TEA sample. This might be due to the secondary phase in that sample. DC electrical conductivity for samples was calculated according to the well-known Arrhenius equation, and the activation energy was estimated to range from 0.39 to 0.075 eV SPH, a behavior dominated by SPH in the high-temperature range, as indicated by the semiconductor behavior of the samples. Because of the effects on structural properties, the kind of fuel utilized is also extremely effective in influencing the catalytic activities of the nanoparticles, according to results of studies conducted to evaluate the electrocatalytic performances of $Bi_{0.9}Ba_{0.1}FeO_3$. After the 4 min trial time, it was found that the CR dye concentration in the solution had nearly entirely deteriorated. When considered collectively and individually, the data show a clear correlation between the kind of fuel and crystallinity and, consequently, between crystallinity and electrocatalytic performance.

Ethical statement

This article does not contain any studies related to animals performed by any of the authors.

Data availability

The data supporting the findings of this article are included in the manuscript and are available upon reasonable request from the corresponding author.

Author contributions

Mohamed Ghozza, Ahmed T. Mosleh: methodology, formal analysis, and data aquration. Tarek A. Yousef, Abdullah Al-Dakhil, Abeer M. Alosaimi, Reda Abdel-Hameed: resources, data analysis, and software: Elbadawy A. Kamoun, H. Zahran, Ibrahim S. Yahia: project management, supervision, wrote original-draft and reviewed the final draft. All authors approved the current and final version of manuscript for submission.

Conflicts of interest

The authors declare that they have no known competing financial interests or personal relationships that could have appeared to influence the work reported in this paper.

Acknowledgements

References

1 J. Silva, A. Reyes, H. Esparza, H. Camacho and L. J. I. F. Fuentes, BiFeO_3: a review on synthesis, doping and crystal structure, *Integr. Ferroelectr.*, 2011, **126**(1), 47–59.

2 J.-C. Chen and J.-M. Wu, Dielectric properties and ac conductivities of dense single-phased BiFeO3 ceramics, *Appl. Phys. Lett.*, 2007, **91**(18), 182903.

3 M. Morozov, N. Lomanova and V. Gusarov, Specific features of BiFeO 3 formation in a mixture of bismuth (III) and iron (III) oxides, *Russ. J. Gen. Chem.*, 2003, **73**, 1676–1680.

4 M. Valant, A.-K. Axelsson and N. J. Alford, Peculiarities of a solid-state synthesis of multiferroic polycrystalline BiFeO3, *Chem. Mater.*, 2007, **19**(22), 5431–5436.

5 C.-H. Yang, T. Koo and Y. Jeong, How to obtain magnetocapacitance effects at room temperature: The case of Mn-doped BiFeO3, *Solid State Commun.*, 2005, **134**(4), 299–301.

6 D. Wang, W. Goh, M. Ning and C. Ong, Effect of Ba doping on magnetic, ferroelectric, and magnetoelectric properties in mutiferroic Bi Fe O 3 at room temperature, *Appl. Phys. Lett.*, 2006, **88**(21), 212907.

7 M. Mehrabi, M. F. Ghasemi, B. Rasti, M. Falahati, A. Mirzaie and A. Hasan, Nanoporous iron oxide nanoparticle: hydrothermal fabrication, human serum albumin interaction and potential antibacterial effects, *J. Biomol. Struct. Dyn.*, 2021, **39**(7), 2595–2606.

8 M. H. Ghozza, I. S. Yahia and M. S. Hussien, Structure, magnetic, and photocatalysis of La0. 7Sr0. 3MO3 (M= Mn, Co, and Fe) perovskite nanoparticles: Novel photocatalytic materials, *Environ. Sci. Pollut. Res.*, 2023, **30**(21), 61106–61122.

9 M. Ghozza and I. Yahia, Impact of gadolinium doping on structure, electrical and magnetic properties of Gd x Cd1−

x MnO3 manganite nanoparticles, *J. Mater. Sci.: Mater. Electron.*, 2021, **32**(9), 11628–11639.

10 M. Mahdavi, M. B. Ahmad, M. J. Haron, Y. Gharayebi, K. Shameli and B. Nadi, Fabrication and characterization of SiO 2/(3-aminopropyl) triethoxysilane-coated magnetite nanoparticles for lead (II) removal from aqueous solution, *J. Inorg. Organomet. Polym. Mater.*, 2013, **23**, 599–607.

11 A. Varma, A. S. Mukasyan, A. S. Rogachev and K. V. Manukyan, Solution combustion synthesis of nanoscale materials, *Chem. Rev.*, 2016, **116**(23), 14493–14586.

12 J. Xiao, Y. Xie, F. Nawaz, Y. Wang, P. Du and H. Cao, Dramatic coupling of visible light with ozone on honeycomb-like porous g-C3N4 towards superior oxidation of water pollutants, *Appl. Catal., B*, 2016, **183**, 417–425.

13 H. Boulahbel, M. Benamira, F. Bouremmad, A. Nada, S. Kiamouche and H. Lahmar, Enhanced photodegradation of Congo red dye under sunlight irradiation by pn NiFe2O4/TiO2 heterostructure, *Inorg. Chem. Commun.*, 2023, 110921.

14 G. S. Kamble and Y.-C. Ling, Solvothermal synthesis of facet-dependent BiVO4 photocatalyst with enhanced visible-light-driven photocatalytic degradation of organic pollutant: assessment of toxicity by zebrafish embryo, *Sci. Rep.*, 2020, **10**(1), 12993.

15 A. Khataee and M. B. J. Kasiri, Photocatalytic degradation of organic dyes in the presence of nanostructured titanium dioxide: Influence of the chemical structure of dyes, *J. Mol. Catal. A: Chem.*, 2010, **328**(1–2), 8–26.

16 M. Saquib and M. Muneer, pigments. TiO2-mediated photocatalytic degradation of a triphenylmethane dye (gentian violet), in aqueous suspensions, *Dyes Pigm.*, 2003, **56**(1), 37–49.

17 G. S. Kamble, T. S. Natarajan, S. S. Patil, M. Thomas, R. K. Chougale and P. D. Sanadi, BiVO4 as a sustainable and emerging photocatalyst: Synthesis methodologies, engineering properties, and its volatile organic compounds degradation efficiency, *Nanomaterials*, 2023, **13**(9), 1528.

18 T. Tapalad, A. Neramittagapong, S. Neramittagapong and M. Boonmee, Degradation of Congo red dye by ozonation, *Chiang Mai J. Sci.*, 2008, **35**(1), 63–68.

19 S. Chakraborty, J. J. Farida, R. Simon, S. Kasthuri and N. Mary, Averrhoe carrambola fruit extract assisted green synthesis of zno nanoparticles for the photodegradation of congo red dye, *Surf. Interfaces*, 2020, **19**, 100488.

20 R. Ahmad and R. J. Kumar, Adsorption studies of hazardous malachite green onto treated ginger waste, *J. Environ. Manage.*, 2010, **91**(4), 1032–1038.

21 Q. Zhang and K. T. Chuang, Adsorption of organic pollutants from effluents of a Kraft pulp mill on activated carbon and polymer resin, *Adv. Environ. Res.*, 2001, **5**(3), 251–258.

22 M. F. Elahmadi, N. Bensalah and A. J. Gadri, Treatment of aqueous wastes contaminated with Congo Red dye by electrochemical oxidation and ozonation processes, *J. Hazard. Mater.*, 2009, **168**(2–3), 1163–1169.

23 R. Kaur and H. Kaur, Electrochemical degradation of Congo red from aqueous solution: role of graphite anode as electrode material, *Port. Electrochim. Acta*, 2016, **34**(3), 185–196.

24 F. Louafi and O. Brahmia, Electrochemical Oxidation Process to the Degradation of Aqueous Solution Dyes, *Sciences B*, 2016, **3**(2), 227–231.

25 M. Chen, W. Ding, J. Wang and G. Diao, Removal of azo dyes from water by combined techniques of adsorption, desorption, and electrolysis based on a supramolecular sorbent, *Ind. Eng. Chem. Res.*, 2013, **52**(6), 2403–2411.

26 A. Del Rio, J. Molina, J. Bonastre and F. J. Cases, Study of the electrochemical oxidation and reduction of CI Reactive Orange 4 in sodium sulphate alkaline solutions, *J. Hazard. Mater.*, 2009, **172**(1), 187–195.

27 N. Bensalah, M. Q. Alfaro and C. Martínez-Huitle, Electrochemical treatment of synthetic wastewaters containing Alphazurine A dye, *Chem. Eng. J.*, 2009, **149**(1–3), 348–352.

28 K. Jüttner, U. Galla and H. Schmieder, Electrochemical approaches to environmental problems in the process industry, *Electrochim. Acta*, 2000, **45**(15–16), 2575–2594.

29 P. Kariyajjanavar, J. Narayana, Y. Nayaka and M. Umanaik, Electrochemical degradation and cyclic voltammetric studies of textile reactive azo dye cibacron navy WB, *Port. Electrochim. Acta*, 2010, **28**(4), 265–277.

30 M. Rivera, M. Pazos and M. Á. Sanromán, Development of an electrochemical cell for the removal of Reactive Black 5, *Desalination*, 2011, **274**(1–3), 39–43.

31 D. Bilican, E. Menéndez, J. Zhang, P. Solsona, J. Fornell and E. Pellicer, Ferromagnetic-like behaviour in bismuth ferrite films prepared by electrodeposition and subsequent heat treatment, *RSC Adv.*, 2017, **7**(51), 32133–32138.

32 C. Ponzoni, M. Cannio, D. Boccaccini, C. Bahl, K. Agersted and C. Leonelli, Ultrafast microwave hydrothermal synthesis and characterization of Bi1− xLaxFeO3 micronized particles, *Mater. Chem. Phys.*, 2015, **162**, 69–75.

33 X. Wang, Y. Zhang and Z. Wu, Magnetic and optical properties of multiferroic bismuth ferrite nanoparticles by tartaric acid-assisted sol–gel strategy, *Mater. Lett.*, 2010, **64**(3), 486–488.

34 E. A. V. Ferri, I. A. Santos, E. Radovanovic, R. Bonzanini and E. M. J. Girotto, Chemical characterization of BiFeO3 obtained by Pechini method, *J. Braz. Chem. Soc.*, 2008, **19**, 1153–1157.

35 V. J. Angadi, I. Yahia, H. Zahran, M. Oliveira, E. Longo and S. Kubrin, Effect of Eu3+ on the structural, magnetic and mössbauer spectroscopy studies of copper ferrite, *J. Magn. Magn. Mater.*, 2022, **562**, 169789.

36 B. Draper, W. L. Yee, A. Pedrana, K. P. Kyi, H. Qureshi and H. Htay, Reducing liver disease-related deaths in the Asia-Pacific: the important role of decentralised and non-specialist led hepatitis C treatment for cirrhotic patients, *Lancet Reg. Health–West. Pac.*, 2022, **20**, 100359.

37 S. J. Kashyap, R. Sankannavar and G. Madhu, Iron oxide (Fe2O3) synthesized via solution-combustion technique with varying fuel-to-oxidizer ratio: FT-IR, XRD, optical and dielectric characterization, *Mater. Chem. Phys.*, 2022, **286**, 126118.

38 G. S. Reddy, H. Sharma, P. Bhaskar and M. Manjunatha, Effect of type of fuel used and calcination temperature on the disorder-order transformation of zinc aluminate spinel during combustion synthesis, *Mater. Chem. Phys.*, 2020, **253**, 123388.

39 T. Lazarova, M. Georgieva, D. Tzankov, D. Voykova, L. Aleksandrov, Z. Cherkezova-Zheleva, *et al.*, Influence of the type of fuel used for the solution combustion synthesis on the structure, morphology and magnetic properties of nanosized NiFe2O4, *J. Alloys Compd.*, 2017, **700**, 272–283.

40 H. Ajamein, M. Haghighi and S. Alaei, The role of various fuels on microwave-enhanced combustion synthesis of CuO/ZnO/Al2O3 nanocatalyst used in hydrogen production via methanol steam reforming, *Energy Convers. Manage.*, 2017, **137**, 61–73.

41 X. Wang, M. Qin, F. Fang, B. Jia, H. Wu and X. Qu, Solution combustion synthesis of nanostructured iron oxides with controllable morphology, composition and electrochemical performance, *Ceram. Int.*, 2018, **44**(4), 4237–4247.

42 E. Novitskaya, J. P. Kelly, S. Bhaduri and O. A. Graeve, A review of solution combustion synthesis: an analysis of parameters controlling powder characteristics, *Int. Mater. Rev.*, 2021, **66**(3), 188–214.

43 A. Cross, S. Roslyakov, K. V. Manukyan, S. Rouvimov, A. S. Rogachev and D. Kovalev, In situ preparation of highly stable Ni-based supported catalysts by solution combustion synthesis, *J. Phys. Chem. C*, 2014, **118**(45), 26191–26198.

44 S. Liu, X. Tan, K. Li and R. Hughes, Synthesis of strontium cerates-based perovskite ceramics via water-soluble complex precursor routes, *Ceram. Int.*, 2002, **28**(3), 327–335.

45 K. Abdouli, W. Cherif, E. Kadri, K. Dhahri, P. Prezas and M. Graça, Structural, electric, and dielectric characterizations of La0. 5Pr0. 2Sr0. 3Mn1− xFexO3 perovskite prepared by self combustion method, *J. Alloys Compd.*, 2018, **739**, 1048–1058.

46 S. Singh and D. Singh, Synthesis of LaFeO 3 nanopowders by glycine–nitrate process without using any solvent: effect of temperature, *Monatsh. Chem.*, 2017, **148**, 879–886.

47 K. Deshpande, A. Mukasyan and A. Varma, Direct synthesis of iron oxide nanopowders by the combustion approach: reaction mechanism and properties, *Chem. Mater.*, 2004, **16**(24), 4896–4904.

48 S. Singh, A. K. Atri, I. Qadir, S. Sharma, U. Manhas and D. Singh, Role of Different Fuels and Sintering Temperatures in the Structural, Optical, Magnetic, and Photocatalytic Properties of Chromium-Containing Nickel Ferrite: Kinetic Study of Photocatalytic Degradation of Rhodamine B Dye, *ACS Omega*, 2023, **8**(7), 6302–6317.

49 J. Toniolo, A. S. Takimi, M. J. Andrade, R. Bonadiman and C. P. J. Bergmann, Synthesis by the solution combustion process and magnetic properties of iron oxide (Fe 3 O 4 and α-Fe 2 O 3) particles, *J. Mater. Sci.*, 2007, **42**, 4785–4791.

50 S. K. Ghosh, A. Prakash, S. Datta, S. K. Roy and D. Basu, Effect of fuel characteristics on synthesis of calcium hydroxyapatite by solution combustion route, *Bull. Mater. Sci.*, 2010, **33**, 7–16.

51 X. Wang, M. Qin, F. Fang, B. Jia, H. Wu and X. Qu, Effect of glycine on one-step solution combustion synthesis of magnetite nanoparticles, *J. Alloys Compd.*, 2017, **719**, 288–295.

52 M. Ghozza, A. T. Mosleh, E. A. Kamoun, M. Abdel-Aty, M. Alfiras and M. H. Ahmed, Nanostructured bismuth ferrite nanoparticles: synthesis, characterization, electrical/magnetic properties and photocatalytic performance, *Phys. Chem. Chem. Phys.*, 2025, **27**(3), 1447–1458.

53 L. Hu, M. Li, L. Cheng, B. Jiang and J. Ai, Solvothermal synthesis of octahedral and magnetic CoFe2O4–reduced graphene oxide hybrids and their photo-Fenton-like behavior under visible-light irradiation, *RSC Adv.*, 2021, **11**, 22250–22263.

54 V. Khomchenko, M. Kopcewicz, A. Lopes, Y. Pogorelov, J. Araujo and J. Vieira, Intrinsic nature of the magnetization enhancement in heterovalently doped Bi1−xAxFeO3 (A= Ca, Sr, Pb, Ba) multiferroics, *J. Phys. D:Appl. Phys.*, 2008, **41**(10), 102003.

55 N. Kambhala, S. Angappane and H. S. Akkera, Structural, Morphological, and Magnetic Properties of Ba, Sm Doped and Ba–Sm Co-Doped BiFeO3 Nanocrystalline Thin Films Deposited by a Spin Coating Method, *Cryst. Res. Technol.*, 2023, 2200261.

56 H. Yan, Z. Chen, L. Zeng, Z. Wang, G. Zheng and R. Zhou, The effect of rGO-doping on the performance of SnO2/rGO flexible humidity sensor, *Nanomaterials*, 2021, **11**(12), 3368.

57 A. M. El Nahrawy, A. Elzwawy, A. B. Abou Hammad and A. Mansour, Influence of NiO on structural, optical, and magnetic properties of Al2O3–P2O5–Na2O magnetic porous nanocomposites nucleated by SiO2, *Solid State Sci.*, 2020, **108**, 106454.

58 K. Souifi, O. Rejaiba, M. Nasri, A. H. Alshehri, J. Khelifi and K. Khirouni, Hopping conduction mechanism and impedance spectroscopy analyses of the half-doped perovsikte Nd0. 5Ba0. 5FeO3 prepared by sol–gel method, *Appl. Phys. A:Mater. Sci. Process.*, 2022, **128**(11), 981.

59 I. Ercan, O. Kaygili, T. Ates, B. Gunduz, N. Bulut and S. Koytepe, The effects of urea content on the structural, thermal and morphological properties of MgO nanopowders, *Ceram. Int.*, 2018, **44**(12), 14523–14527.

60 M. El-Desoky, M. Mostafa, M. Ayoub and M. J. Ahmed, Transport properties of Ba-doped BiFeO 3 multiferroic nanoparticles, *J. Mater. Sci.: Mater. Electron.*, 2015, **26**, 6793–6800.

61 S. Sagar and M. Anantharaman, On conduction mechanism in paramagnetic phase of Gd based manganites, *Bull. Mater. Sci.*, 2012, **35**, 41–45.

62 R. Bhowmik, Dielectric and magnetic study of BaTi0. 5Mn0. 5O3 ceramics, synthesized by solid state sintering, mechanical alloying and chemical routes, *Ceram. Int.*, 2012, **38**(6), 5069–5080.

63 M. Al-Assiri, M. Mostafa, M. Ali and M. El-Desoky, Synthesis, structural and electrical properties of annealed ZnO thin films deposited by pulsed laser deposition (PLD), *Superlattices Microstruct.*, 2014, **75**, 127–135.

64 D. P. Dutta, O. Jayakumar, A. Tyagi, K. Girija, C. Pillai and G. Sharma, Effect of doping on the morphology and multiferroic properties of BiFeO 3 nanorods, *Nanoscale*, 2010, **2**(7), 1149–1154.

65 N. Kambhala, S. Angappane, S. Thiyagaraj and H. S. Akkera, Structural and Magnetic Properties of Bi0. 9Ba0. 1FeO3 and Bi0. 9Ba0. 05Sm0. 05FeO3 Nanoparticles, *J. Supercond. Novel Magn.*, 2023, **36**(1), 223–228.

66 *Enhancement of Ferromagnetic and Dielectric Properties of Nanostructured Barium Doped Bismuth Ferrite Fabricated by Facile Hydrothermal Route*, AIP Conference Proceedings, ed. Chaudhuri A. and Mandal K., 2015.

67 M. Li, M. Ning, Y. Ma, Q. Wu and C. J. Ong, Room temperature ferroelectric, ferromagnetic and magnetoelectric properties of Ba-doped BiFeO3 thin films, *J. Phys. D: Appl. Phys.*, 2007, **40**(6), 1603.

68 A. Gautam and V. Rangra, Technology. Effect of Ba ions substitution on multiferroic properties of BiFeO3 perovskite, *Cryst. Res. Technol.*, 2010, **45**(9), 953–956.

69 S. R. Khan, S. Jamil, S. Bibi, S. Ali, T. Habib and M. R. S. A. J. Janjua, A versatile material: perovskite bismuth ferrite microparticles as a potential catalyst for enhancing fuel efficiency and degradation of various organic dyes, *J. Inorg. Organomet. Polym. Mater.*, 2020, **30**, 3761–3770.

70 A. A. Gungor, H. Nadaroglu and D. D. Gultekin, Synthesis and characterization of nano-strontium oxide (SrO) Using erzincan cimin grape (Vitis vinifera, Cimin), *Chem. Sci. Int. J*, 2019, **26**(3), 1–7.

71 E. Z. El-Ashtoukhy and N. Amin, Removal of acid green dye 50 from wastewater by anodic oxidation and electrocoagulation—A comparative study, *J. Hazard. Mater.*, 2010, **179**(1–3), 113–119.